Plasma Chemistry and Plasma Processing, Vol. 16, No. 2, 1996

Homogeneous Nucleation of Metals in a Plasma-Quench Reactor

Randall A. LaViolette,[1] Ray A. Berry,[1] and Robert McGraw[2]

Received April 20, 1995; revised June 10, 1995

*We present a new and general application of the method of moments for modeling the nucleation of condensates in a steady-state supersonic nozzle flow generated in a plasma-quench reactor. A closed set of growth/evaporation rate equations has been employed to propagate the moments of the particle size distribution without invoking the usual coarse-graining or truncation approximations of conventional binning approaches. The method has been employed to calculate the nucleation rates, particle number density, and the particle-size distribution for 11 elemental metals (*Ag, Al, Be, Ce, Cr, Fe, Gd, Ti, Th, U, *and* Zr*) condensing in a model argon nozzle flow. We have identified the regions in the nozzle of maximum nucleation rate, and have shown how different particle-size distributions can develop in different regions.*

KEY WORDS: Homogeneous nucleation; metal vapors; supersonic flow nozzle; plasma quench reactor.

1. INTRODUCTION

A plasma quench reactor (PQR) combines a plasma torch with an expansion chamber (either a nozzle or a free jet) so that the reactions which occur in the high-temperature region around the torch are quenched in the expansion chamber.[1,2] In a recent application, a PQR produced a pure metal powder by cracking a metal compound in a plasma torch, followed by condensing the metal vapor in a nozzle, where the sudden expansion adiabatically cools the gas and quenches any back reactions.[3,4] We consider here only the problem of the condensation of metals in the nozzle of a model PQR that follows the scenario above. We ask the following: What are the nucleation rates in the nozzle? What fraction of the metal vapor condenses

[1]Idaho National Engineering Laboratory, P.O. Box 1625, Idaho Falls, Idaho 83415-2208.
[2]Brookhaven National Laboratory, Upton, New York 11973.

0272-4324/96/0600-0249$09.50/0

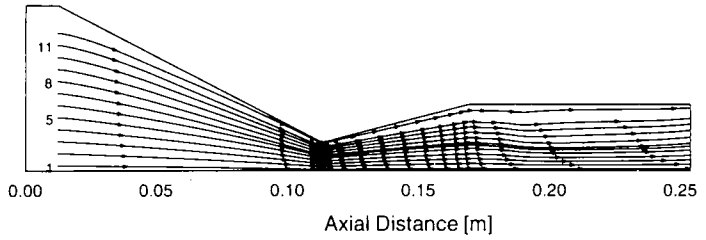

Fig. 1. Cross-section of the top half of the PQR nozzle, with streamlines calculated for the steady-state argon flow. Labels (1, 5, 8, 11) mark streamlines referred to in the text and Figs. 5–7. The aspect ratio is exaggerated by a factor of 10 for clarity. The plasma torch (not shown) is placed behind the nozzle inlet.

in the nozzle? and What is the size distribution of the primary particles at the nozzle exit?

In order to answer these questions, we have combined a computational fluid dynamics (CFD) description of the axisymmetric flow of argon gas in a model nozzle PQR (see Fig. 1) with a new application of the method of moments for homogeneous nucleation in a flow. In the calculations we treat the metal as a tracer in the argon flow, injected on a streamline near the nozzle inlet, as though it had already been cracked. We also assume that its condensation does not perturb the flow, i.e., the metal is a tracer in either the vapor or condensed phase. The former treatment is reasonable in view of the high temperatures found in the plasma portion of the flow, and the latter is reasonable in view of the small size and concentration of the particles obtained. Finally, in view of the low mixing between streamlines, we treat the nucleation along one streamline as independent of any other.

The following section provides the development of the nucleation theory. Section 3 presents the details of the computations, with the results presented in Section 4. Section 5 concludes this work with a summary of the results.

2. NUCLEATION THEORY OF CONDENSATION IN A FLOW

We begin by extending the method-of-moments description of nucleation in a continuously stirred tank reactor developed by McGraw and Saunders[5] to the problem of nucleation in a nozzle flow. The growth and evaporation of nucleating particles is described by the system of coupled differential equations[6]

$$\frac{\partial \rho_n}{\partial t} = \frac{\rho_n}{\rho}\frac{\partial \rho}{\partial t} + W_{n-1,n} - W_{n,n+1} \tag{1}$$

where ρ_n is the particle-size distribution, i.e., the number density of particles of size n, and ρ is the carrier gas density. The $W_{m,n}(\rho_1, \rho_m, \rho_n)$ are the net fluxes for formation of particles of size n from particles of size m. Equation (1) results from employing the usual assumption that particles grow or evaporate only by monomer addition or subtractions respectively, i.e., $W_{n\pm k,n} = W_{n,n\pm k} = 0$ for $k \geq 2$. The lead term on the right-hand side of Eq. (1) derives from the continuity equations (Section 3 below) and gives the contribution to the change in particle number density due to changes in the flow.

Where the fully time-dependent solutions are required, as in our study, the theory follows one of two paths when going beyond simplified analytic models. In the first, it is recognized that the system above involves an intractable number of equations, corresponding roughly to the number of molecules present in the particles of largest size (a number not known *a priori*), and therefore is impossible to solve as it stands. Therefore some truncation criterion is invoked in combination with a binning procedure that groups all particles of a certain size range together. Typically the bin size grows geometrically with particle size. In this way the large number of cluster sizes is reduced to a few coarse-grained bin sizes that are required to be tracked in the flow. Bin methods have been employed in other studies of nucleation in plasma processing.[7,8] In the bin approach the major issues are how to best represent evaporation and growth processes, and how to optimize the assignment of the bin sizes so as to obtain the required bin resolution while at the same time keeping the total number of bins small enough to facilitate tracking even in complex hydrodynamic flows.

Here we exploit an alternate approach to the description of aerosol nucleation and growth dynamics known as the method of moments.[5,9] In this method, the large number of equations for ρ_n are replaced by a few equations for the moments of the size distribution, the kth moment m_k being defined by

$$m_k \equiv \sum_{n=1} n^{k/3} \rho_n \tag{2}$$

Here the relevant issues are how best to extract required size distribution information from the moments, which are computed directly, and how to ensure that the evolution equations remain in closed form. We will show that under certain closure conditions formally exact solutions for the evolution of particle size and number density in the PQR can be obtained.

For the case of free molecular growth, i.e., where the particle radius is less than the mean free path of the carrier gas, Eq. (1) can be contracted exactly into a closed system of only four coupled nonlinear equations, without any truncation or coarse-graining of the particle size distribution.

These moment equations for the particle distribution are[5]

$$\frac{\partial m_0}{\partial t} = \frac{m_0}{\rho}\frac{\partial \rho}{\partial t} + J(\rho_1)$$

$$\frac{\partial m_k}{\partial t} = \frac{m_k}{\rho}\frac{\partial \rho}{\partial t} + \frac{k}{3}\frac{m_{k-1}}{\tau}\frac{(S-1)}{S}, \qquad k \geq 1 \tag{3}$$

$$\frac{\partial \rho_1}{\partial t} = \frac{\rho_1}{\rho}\frac{\partial \rho}{\partial t} - \frac{m_2}{\tau}\frac{(S-1)}{S}$$

where J is the nucleation rate, S is the monomer supersaturation ratio, and τ is the time between monomer collisions. The supersaturation is defined by $S \equiv \rho_1/\rho_1^{eq}$, where the equilibrium concentration ρ_1^{eq} is determined from the condensate vapor pressure and the ideal-gas equation of state. The kinetic theory of gases gives τ through

$$\tau^{-1} = \sqrt{\frac{k_B T}{2\pi m_1}}\, s_1 \rho_1 \tag{4}$$

where k_B is the Boltzmann constant, s_1 is the monomer surface area, and m_1 is the monomer mass. For an accommodation coefficient of unity (which we use here), $(s_1\tau)^{-1}$ gives the free molecular rate of accommodation, from which one can derive Eq. (3).[5] The extra factor of $(S-1)/S$ in Eq. (3) is included here to partially correct for particle evaporation in the growth stages. This is only a partial correction because curvature effects on the evaporation rate are neglected to facilitate closure of the moment equations. Note that in the nucleation cluster size regime, where curvature effects are most pronounced, they are automatically accounted for in the classical expression for the nucleation rate. The correction is small in regions where S is large, i.e., where the nucleation rate is high, and these are the principal regions of interest. Closure is achieved with only four equations ($k \leq 2$ above) because the equation for the monomer involves m_2 but no higher moments. However, the sequence is readily continued for tracking higher-order moments of the particle size distribution if these are desired because the time derivative of m_k depends only on m_k and m_{k-1}.

In order to minimize the number of physical properties required to determine the nucleation rates of metal vapors at elevated temperatures, we employ the classical theory due to Becker, Doring, and Zeldovich for nucleation rates as expressed in corresponding-states form[10]

$$J(\rho_1) = \frac{\Gamma \rho_1 2^{1/6}}{\tau}\sqrt{\frac{\Theta}{6\pi}}\exp\left(-\frac{\Theta^3}{(\ln S)^2}\right) \tag{5}$$

The dimensionless corresponding-states parameter Θ is defined by

$$\Theta = \frac{\sigma}{k_B T}\left(\frac{16\pi v_1^2}{3}\right)^{1/3} \tag{6}$$

where T is the absolute temperature, v_1 is the monomer volume, and σ is the condensed phase surface tension. In order to make contact with more modern theories for J, the replacement factor Γ is included in Eq. (5). For example, in the Reiss–Katz–Cohen theory, Γ may be as large as 10^6.[11] We retain the classical choice of $\Gamma = 1$ here because we have observed little difference between the results of the two theories, although in other applications the choice of Γ might become important.

Finally, in order to adapt the moment equations to nucleation in a steady-state flow, we transform the time dependence of the moments into a path dependence, where the path s is the length along a selected one-dimensional streamline of the flow. Then Eq. (3) becomes

$$\begin{aligned}
\frac{\partial m_0}{\partial s} &= \frac{m_0}{\rho}\frac{\partial \rho}{\partial s} + \frac{J(\rho_1)}{u_s} \\
\frac{\partial m_k}{\partial s} &= \frac{m_k}{\rho}\frac{\partial \rho}{\partial s} + \frac{k}{3}\frac{m_{k-1}}{u_s \tau}\frac{(S-1)}{S}, \qquad k \geq 1 \\
\frac{\partial \rho_1}{\partial s} &= \frac{\rho_1}{\rho}\frac{\partial \rho}{\partial s} - \frac{m_2}{u_s \tau}\frac{(S-1)}{S}
\end{aligned} \tag{7}$$

where u_s is the gas velocity at s along the streamline.

Frequently one is interested only in integrated properties of an aerosol distribution that can be approximated directly from the lower-order moments of the size distribution without requiring the distribution itself. However, here we are interested in examining the distribution itself. There are efficient and accurate moment inversion algorithms available which approximate the distribution from its lower-order moment sequence. Of these, we prefer here a continuous representation of the size distribution consistent with the known moments. The least biased distribution available that meets these criteria is provided by the maximum entropy inversion.[12,13] This method furnishes the unique distribution function having the least bias (maximum entropy) subject to the constraint that the known moments are exactly reproduced. The maximum-entropy expression for the reconstructed particle-size distribution ϕ_N knowing only the first $N+1$ moments is

$$\phi_N(x; \lambda_0, \ldots, \lambda_N) = \exp\left(1 - \sum_{j=0}^{N} \lambda_j x^j\right) \tag{8}$$

where x is the continuous variable that represents the particle size, and the λ_j are the Lagrange multipliers found by solving the nonlinear system

$$m_k = \int_0^\infty dx\ \phi_N(x; \lambda_0, \ldots, \lambda_N) x^k, \qquad k = 0, \ldots, N \tag{9}$$

where m_k are the known moments. Our experience shows that converged maximum entropy distributions can be obtained with only a few moments beyond the required $N = 2$, i.e., with $4 \leq N \leq 6$.

3. COMPUTATIONS

The nozzle flow of hot argon gas was described with the Reynolds-averaged Navier–Stokes equations. In integral form, employing summation convention, these equations are

$$\frac{\partial}{\partial t} \int_V U\, dV + \int_A F_1 \mathbf{i} \cdot \mathbf{n} + F_2 \mathbf{j} \cdot \mathbf{n} + F_3 \mathbf{k} \cdot \mathbf{n}\, dS = 0 \tag{10}$$

where

$$U \equiv \begin{pmatrix} \rho \\ \rho u_1 \\ \rho u_2 \\ \rho u_3 \\ E \end{pmatrix}, \qquad F_i \equiv \begin{pmatrix} \rho u_i \\ \rho u_i u_1 + p\delta_{1i} - \tau_{i1} \\ \rho u_i u_2 + p\delta_{2i} - \tau_{i2} \\ \rho u_i u_3 + p\delta_{3i} - \tau_{i3} \\ (E+p)u_i - u_j \tau_{ij} + q_i \end{pmatrix} \tag{11}$$

$\int_S$ indicates a surface integral with unit normal $\mathbf{n}$ and $\int_V$ indicates a volume integral. Also, p is the pressure, $E = \rho(e + u_j u_j/2)$ is the total energy per unit volume, e is the internal energy per unit mass, the τ_{ij} are the full viscous shear stresses, and q_i is the total heat transfer rate. The conservative form of the Navier–Stokes equations are solved using a time-marching (to steady state) finite volume method. Inviscid fluxes are calculated at finite volume surfaces using the second-order upwind-biased flux-splitting scheme of Harten and Yee,[14] which in turn is based on the flux-difference splitting method of Roe.[15] Flux limiting is incorporated in order to avoid oscillations. The viscous fluxes are calculated at the volume faces with standard second-order central differences. These CFD simulations employed an implicit time-differencing scheme with a (lower, upper)-symmetrical-Gauss–Seidel algorithm.[16,17] These calculations were carried out with the above techniques as embodied in the INCA™ code.[18]

The top half of our axisymmetric nozzle is shown with streamlines in Fig. 1. The half nozzle was simulated with 129×39 volumes in the axial and radial directions, respectively. We employed the Baldwin–Lomax turbulence model[19] with a Blottner-type temperature-dependent viscosity formula and a no-slip boundary condition for the wall. We assumed that the nozzle wall was isothermal at a temperature of 1000 K. Our inlet conditions were specified by a stagnation pressure of 413.5 kPa and a stagnation temperature of 9000 K. This gives a mean flow rate of about 50 moles per hour of argon gas.

Note that the first of the set of Navier–Stokes equations is the continuity equation

$$\frac{\partial \rho}{\partial t} = -\nabla \cdot (\rho u) \tag{12}$$

This is the only member of the set that appears explicitly in Eq. (3) for describing the condensation of a trace species in the flow. Of course, evaluation of Eq. (12) requires solution of the full set of Navier–Stokes equations. However, because the analysis is limited to trace condensing species, there is no reverse feedback from nucleation and growth processes back to the flow. This simplification permits arbitrary changes in the vapor/condensate conditions for a given set of flowfield conditions (e.g., temperatures, pressures, velocities, etc.) without having each time to recalculate the flow. In order to exploit this feature, the partial derivative on the left-hand side of Eq. (12) is evaluated from Eqs. (10) and (11) only once for each flow field condition. The streamline information, needed for evaluation of the leading terms on the right-hand side of Eq. (7), is obtained using standard spline interpolation methods. The interpolation is applied to the tabulated numerical output along each streamline generated by the flow field simulation code. Finally, changes in metal vapor composition are handled through a new integration of Eq. (7), using the stored trajectory information describing the fixed conditions of the flow.

Mixing between streamlines was not neglected in our flow field simulation because the Baldwin–Lomas model was in place. However, once the flow field was determined, we observed that mixing between the streamlines did not occur to an appreciable extent. Consequently we were able to simplify the calculations significantly by neglecting mixing in the nucleation and growth part of the calculations based upon the method of moments.

The connection between the flow field simulation described above and Eq. (7) for the nucleation rate and particle-size moments can now be made explicit. The gas dynamics calculations track the flow field parameters T, u_s, and ρ along each streamline of the nozzle flow for input into Eq. (7). Thus, the time between monomer collisions τ and the nucleation rate J each

depends on the flow field parameters T and ρ_1 through Eqs. (4)–(6). Equation (7) is solved along each streamline given by the flow field simulation using an adaptive Runge–Kutta algorithm.[20] The vapor pressures are taken from a universal empirical fit.[21] The surface tension for each of the condensing metals considered here is taken from fits to experiment.[22] We chose the critical temperature T_c to be temperature at which the extrapolated surface tension vanishes. This appears to be a reasonable approach in view of the uncertain status of estimates for T_c.[23] Liquid-state values were chosen under the assumption that the metal initially condenses to that phase. If, at the point of nucleation, the solid phase is thermodynamically favored, the nucleation step itself may still proceed through the liquid phase as suggested by the Ostwald rule of stages.[24] The variation of the liquid-phase metal density with temperature was also taken from an empirical fit.[22]

The computations are not especially demanding. The CFD calculations for the flow field require less than 6 h on a desktop workstation, and frequently converge in 2 h. The subsequent solution of the moment equations on the streamlines takes only about 1 min for each condensate on each streamline. Although both calculations employed double precision, each required fewer than the 32Mb of RAM installed on most desktop workstations. These observations suggest that a high-end personal computer would have been adequate for any of the calculations presented here.

4. RESULTS

The results of the CFD simulation of the argon gas flow in the nozzle are shown in Fig. 2, displaying the steady-state gas temperature, density, and Mach number, respectively. The gas is heated by a plasma torch placed before the nozzle inlet. The initially hot subsonic gas expands and cools rapidly after passing through the throat of the nozzle. The gas recompresses and reheats somewhat as it passes through the tailpipe of the nozzle, before once again expanding and cooling as it exits the nozzle. Its density minimum is achieved in two tori where the diverging part of the nozzle meets the tailpipe. In the diverging part of the nozzle, the gas flow is supersonic, but in the upper portion of the tailpipe, the gas becomes subsonic again. A tracer introduced near the nozzle inlet exits the nozzle in about 1 ms for the streamlines nearest the center, and up to 2 ms for the streamlines nearest the nozzle wall. The residence time for condensed particles (measured from the region of maximum nucleation rate to the nozzle exit) is about one order of magnitude shorter than the tracer residence time.

We examined nucleation on each of the 12 independent streamlines for the following 11 species: Al, Ag, Be, Ce, Cr, Fe, Gd, Ti, Th, U, and Zr.

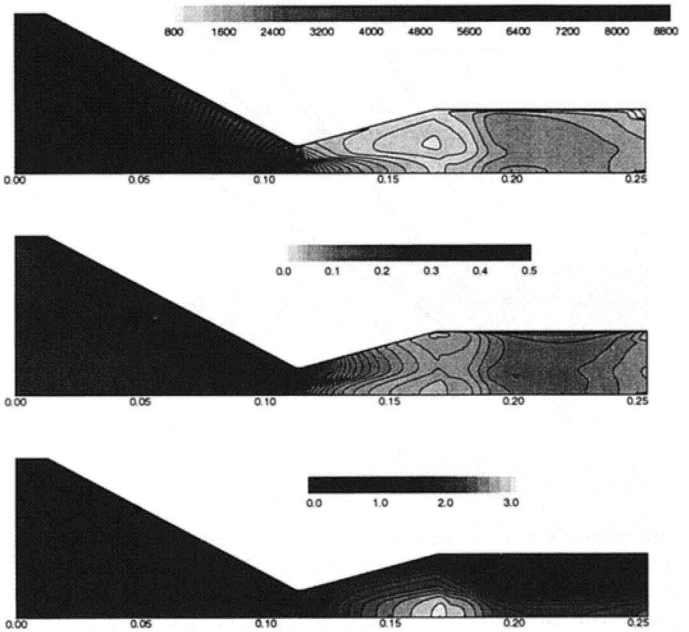

Fig. 2. Properties of the steady-state argon flow in the PQR nozzle. The top panel shows the temperature (K), the middle panel shows the density (kg/m^3), and the bottom panel shows the Mach number. All of these were interpolated onto the CFD mesh.

For each streamline the initial steady-state concentration of metal vapor was set to 0.5 mole/h, or $X = 0.01$ mole fraction of the carrier gas. Under these conditions, Cr, Fe, and U do not condense appreciably anywhere inside the nozzle. Thorium is the most rapidly and completely condensing of any of these metals.

The corresponding-states (CS) correlation for the homogeneous nucleation thresholds of supercooled vapors[10] can be used to provide a collective overview of the nucleating properties of supercooled metal vapors as shown in Fig. 3. The figure shows the logarithm (base 10) of the critical supersaturation ratio S_c (defined as the supersaturation ratio S for which the nucleation rate J is unity) plotted against a function of the reduced temperature $T^* = T/T_c$, where T_c is the estimated critical temperature for the metal. The open symbols are taken from the simulation data for each of the tested metals, along each of the streamlines, and mark the conditions where the calculated nucleation rate, obtained using the full Becker–Doring–Zeldovich theory [Eq. (5)], is 1 cm^{-3} s^{-1}. For this calculation we included results collected for $X = 0.02$ as well as $X = 0.01$. The CS correlation has been refined by the

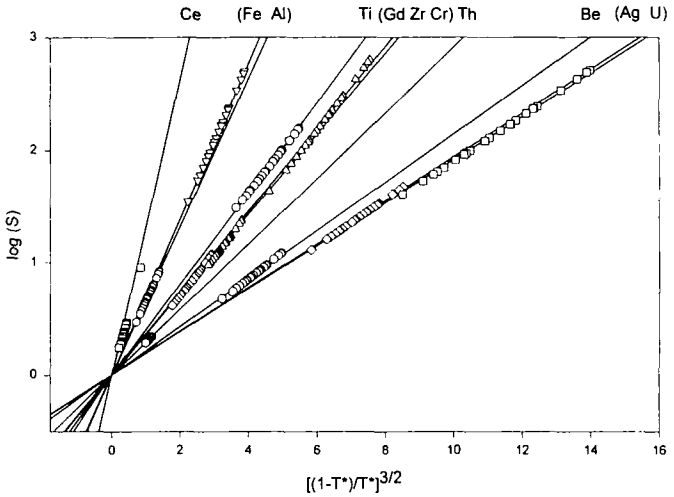

Fig. 3. Corresponding-states diagram for the metals nucleating in the PQR nozzle, where $T = T/T_c$. The supersaturation S and reduced temperature T correspond to the onset of nucleation, i.e., where $J = 1\ \text{cm}^{-3}\ \text{s}^{-1}$. The data were collected for each metal on each streamline for two sets of metal vapor concentrations: $X = 0.01$ and $X = 0.02$. The different shapes used for the symbols distinguish between metals that nearly overlap in the diagram. The lines were determined by a least-squares fit of the data through the origin.

introduction of a universal temperature dependence[25,26] given by

$$\log(S_c) = C\left(\frac{T_c}{T} - 1\right)^{3/2} \tag{13}$$

An expression for C is given explicitly by Hale;[26] here we regard C only as a constant to be determined by a least-squares fit. The regression lines through the origin confirm the predicted nucleation behavior from the CS theory for each of the metals. Figure 3 clearly displays the excellent agreement between the CS predictions and the full multiparameter Becker–Doring–Zeldovich theory employed in the simulations.

We chose Ti for further examination of its nucleation behavior in the PQR. Ti lies in the middle of the corresponding-states diagram in Fig. 3, and for initial $X = 0.01$ its condensation behavior is between the two extremes of negligible and complete condensation within the nozzle. Figure 4 shows, in three panels, the logarithm (base 10) of the nucleation rate along each of the streamlines, the logarithm (base 10) of the particle number density (particles/cm^3), and the fraction of Ti condensate, respectively. For the sake of clarity we have interpolated the results for the particle number density and the condensate fraction onto the CFD simulation mesh, even though

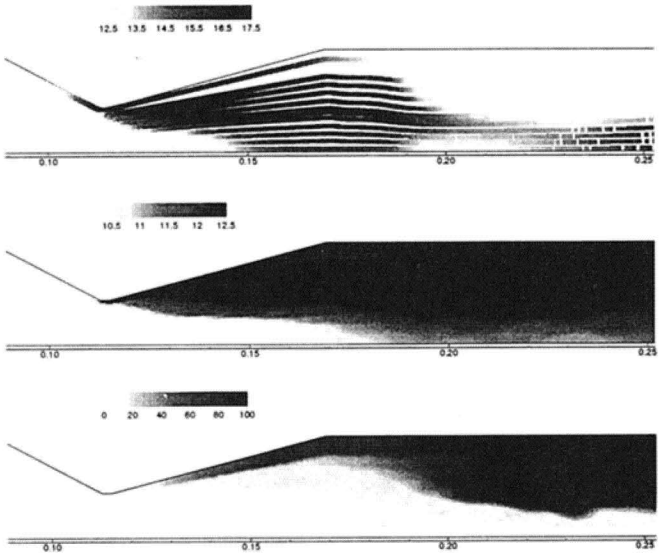

Fig. 4. Properties of the condensing metal in the PQR nozzle. The top panel shows the log (base 10) of the nucleation rate along the 12 streamlines. The middle panel shows the log (base 10) of the particle density (number of condensed particles per cm^{-3}), also taken from the streamlines but for clarity interpolated onto the CFD mesh. The bottom panel shows the percent of metal vapor that has condensed, also interpolated onto the CFD mesh.

the results are computed only along the streamlines. The region of maximum nucleation rate is an annular shaped volume near the nozzle throat, and closer to the wall than to the center. This region does not coincide with any of the temperature, density, or speed minima or maxima displayed in Fig. 2. Within the nozzle there appear to be two regions of nucleation, the former containing the maximum nucleation rate near the throat of the nozzle, and a second, much less pronounced region in the tailpipe near the center of the nozzle. Comparison with the lowest panel of Fig. 4 shows that there is little or no nucleation in the region where Ti has completely condensed out of the Ti vapor.

These simulations track the evolution of condensed metal formation through the stage of primary particle formation. Secondary stages of particle evolution, including coagulation and, at elevated temperatures, fusion, do not occur significantly here because of the short ($\leq 100\ \mu s$) time scale of the nozzle expansion. However, with aging of the aerosol further downstream (i.e., past the nozzle exit), particle aggregates will begin to dominate the particle size distribution. Growth by vapor condensation is generally a much faster process than coagulation, resulting, for all the cases we have studied,

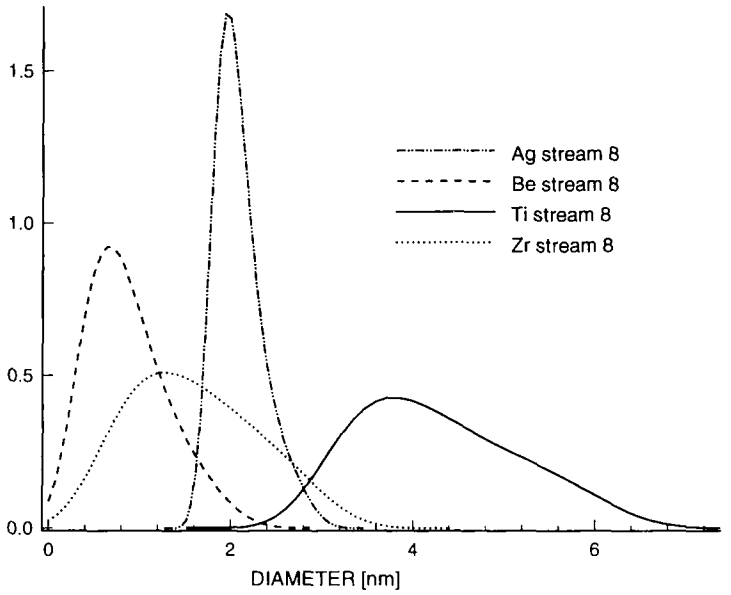

Fig. 5. Normalized particle size distributions for four selected metals, taken at the exit of streamline 8.

in a well-defined separation of time scales for these processes. Thus nucleation and growth processes, which govern the primary aerosol, are generally completed well before significant interparticle interaction has had time to take place. Therefore, a two-stage approach can be employed when simulation of the secondary aerosol is required. First, our moment evolution equation can be employed to simulate the primary aerosol, as demonstrated here, followed by application of standard coagulation models[27] to obtain the distribution of aggregates at the latter stages of the flow. Formulas in Ref. 27 also provide a rule of thumb that indicates that for most of the metals considered here, the particle number density (cf. Fig. 4) would have to increase by a factor of between 5 and 10 for coagulation to begin within the nozzle.

Figures 5–7 each show the four-moment maximum entropy reconstruction of the size distribution of the primary condensed particles, taken at the exit of the nozzle, in those regions where the metal is nearly completely condensed. Figure 5 shows results for selected species where streamline 8 (cf. Fig. 1) exits the nozzle. Here, each species has completely condensed out of its vapor. Silver displays the most monodisperse particle distribution. Beryllium has the highest nucleation rates, and so not surprisingly grows

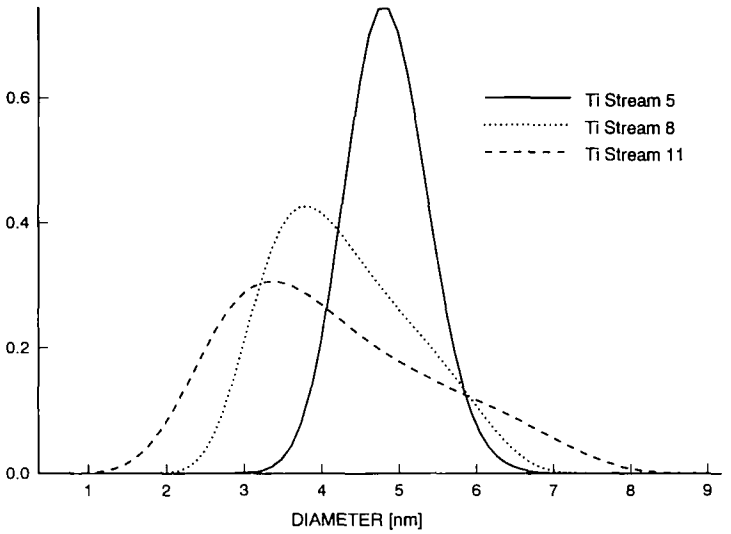

Fig. 6. Normalized particle size distributions for Ti ($X=0.01$) for three different streamlines at the nozzle exit.

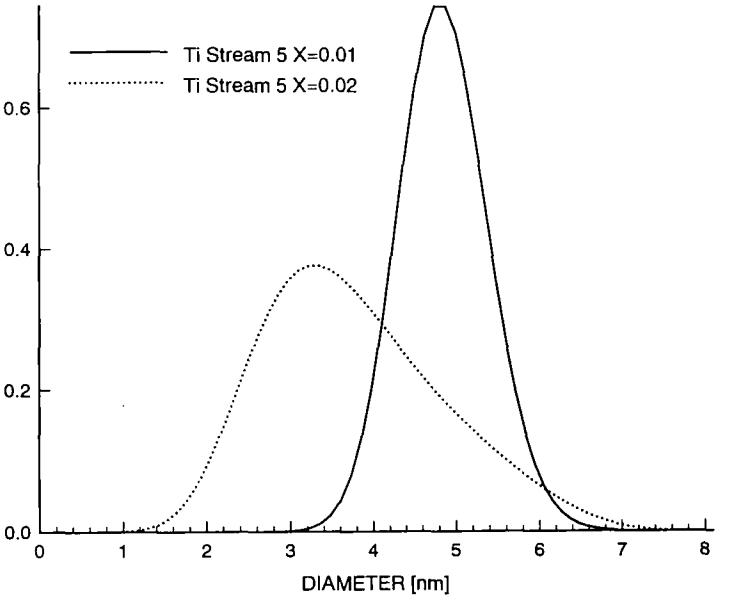

Fig. 7. Normalized particle size distributions for Ti (streamline 5) for two different vapor concentrations ($X=0.01$ and $X=0.02$).

the smallest particles. Zirconium and titanium are more complicated, however. Both give relatively broad, polydisperse distributions. Figure 6 shows, for Ti, the variation in the particle size distribution at the nozzle exit with streamline. Streamlines 1–4 would not yield meaningful particle size distributions because the condensation is negligible there. A relatively narrow distribution is found for streamline 5, and the broader distributions are found for both streamlines 8 and 11. Finally, Fig. 7 shows, again for Ti, the variation in the particle size distribution along one streamline with initial concentration. Doubling the initial concentration raises the nucleation rates, gives a smaller average particle size, and a larger particle size dispersion.

Monodisperse distributions (e.g., Ag above) occur when the nucleation time is short, i.e., nucleation occurs in a burst, because all the particles that start at nearly the same time grow to nearly the same size. Broader distributions and multimodal distributions (e.g., Ti and Zr above) are the result of nucleation occurring over longer periods of time or over different periods of time. In general, the particle size distributions are shaped by the (nonlinear) physics contained in Eq. (7), which in turn employs the complicated temperature, density, and velocity behavior of the streamline trajectories generated in the flow field. Consequently, there are no simple methods available to predict these distributions, other than to execute the model itself.

A direct comparison of these results is not yet possible because neither the model nozzle configuration nor the flow conditions match those of any experiment reported so far. However, an experimental PQR has produced Ti particles with an average diameter of about 5 nm, comparable to the results presented above for Ti.[4]

5. CONCLUSIONS

We have developed a method that models nucleation and growth of condensing particles in a steady-state nozzle flow in order to assist the design and optimization of plasma quench reactors for advanced materials processing. This method combines a closed moments treatment of the nucleation rate equations with a complete CFD treatment of the gas dynamics of the flow. We connected these two approaches by treating the condensing particles as tracers following independent streamlines computed for the flow. The method requires no more computing resources than those required to compute the flow field itself.

We have applied this method to a variety of metals condensing under test flow conditions generated in a model plasma quench reactor. We have calculated the onset position and rate of nucleation, the particle number density and size, the fraction of metal vapor condensed inside the reactor, and the particle size distribution as a function of position inside the reactor.

We have observed that some metals condense rapidly and completely inside the reactor, while others do not condense in any appreciable fraction anywhere inside the reactor. We have also observed that growth, evaporation, and nucleation of the particles are strongly coupled. The highest nucleation rates are found throughout a small but significant annular volume inside the reactor. The fact that this volume does not coincide with any special feature (minima or maxima) of the temperature, density, or speed in the flow field is an indication of the complexity of condensation processes represented in Eq. (7), i.e., nucleation depends on several factors simultaneously including inhibitory feedback from vapor depletion due to particle growth. The distribution of nucleation rates inside the nozzle contributes to the polydispersity of the calculated particle size distribution. Furthermore, the particle size distribution at the nozzle exit is strongly sensitive to the type of metal being condensed, and its concentration. Finally, all of these details are sensitive to the radial position of the streamline, and configuration of the gas flow field itself, which in turn is determined by the initial gas conditions and the shape of the reactor nozzle.

ACKNOWLEDGMENT

This work was supported through the INEL Long-Term Research Initiative under DOE Idaho Operations Office Contracts DE-AC07-76ID01570 and DE-AC07-94ID13223, and NASA Agreement W-18429 under DOE Chicago Operations Office Contract DE-AC02-76CH00016.

REFERENCES

1. S. V. Joshi, Q. Liang, J. Y. Park, and J. A. Batdorf, *Plasma Chem. Plasma Process.* **10**, 339 (1990).
2. H. Ageorges, S. Megy, J.-M. Baronnet, and J. K. Williams, *Plasma Chem. Plasma Process.* **13**, 613 (1993).
3. J. W. Sears, A. D. Donaldson, and J. D. Grandy, *Advances in Powder Metallurgy and Particulate Materials*, Vol. 1, S. Lall and A. J. Neupaver, eds., Metal Powder Industries Federation, Princeton, New Jersey (1994), p. 169.
4. S. G. Hutchison, C. M. Wai, J. Dong, and R. J. Kearney, *Plasma Chem. Plasma Process.* **15**, 353 (1995).
5. R. McGraw and J. H. Saunders, *Aerosol Sci. Technol.* **3**, 367 (1984).
6. W. G. Courtney, *J. Chem. Phys.* **36**, 2009 (1962).
7. S. L. Girshick and C.-P. Chiu, *Plasma Chem. Plasma Process.* **9**, 355 (1989).
8. J. S. McFeaters, R. L. Stephens, P. Schwerdtferger, and M. Liddell, *Plasma Chem. Plasma Process.* **14**, 333 (1994).
9. H. M. Hulbert and S. Katz, *Chem. Eng. Sci.* **19**, 555 (1964).
10. R. McGraw, *J. Chem. Phys.* **75**, 5514 (1981).
11. H. Reiss, J. L. Katz, and E. R. Cohen, *J. Chem. Phys.* **48**, 5553 (1968).
12. E. T. Jaynes, *Phys. Rev.* **106**, 620 (1957).

13. J. Einbu, *IEEE Trans. Inform. Theory* **IT-23**, 772 (1977).
14. H. C. Yee, R. F. Warning, and A. Harten, *J. Comput. Phys.* **57**, 327 (1985).
15. P. L. Roe, *J. Comput. Phys.* **43**, 357 (1981).
16. S. Yoon and A. Jameson, AIAA paper 87-0600 (1987).
17. S. T. Imlay, D. W. Roberts, and M. Soetrisno, AIAA paper 91-2153 (1991).
18. S. T. Imlay, INCA™: *3D Multi-Zone Navier–Stokes Flow Analysis with Finite-Rate Chemistry, version 1.2*, Amtec Engineering Inc., Bellevue, Washington (1994).
19. B. Baldwin and H. Lomax, AIAA paper 78-257 (1978).
20. W. H. Press, S. A. Teukolsky, W. T. Vetterling, and B. P. Flannery, *Numerical Recipes in Fortran*, 2nd edn., Cambridge University Press, New York (1992).
21. C. Codegone, *Int. J. Heat Mass Transfer* **14**, 565 (1971).
22. *Smithells Metals Reference Book*, 7th edn., E. A. Brandes and G. B. Brook, eds., Butterworth-Heinemann, Oxford (1992).
23. R. W. Ohse and H. von Tippelskirch, *High Temp. High Press.* **9**, 367 (1977). Note that estimates in the literature for T_c for some of these metals vary among themselves by a factor of two or more.
24. H. R. Pruppacher and J. D. Klett, *Microphysics of Clouds and Precipitation*, Reidel, Boston, Massachusetts (1980).
25. D. H. Rasmussen and S. V. Babu, *Chem. Phys. Lett.* **108**, 449 (1984).
26. B. N. Hale, *Phys. Rev. A* **33**, 4156 (1986); this form was first presented in 1982 at the 56th Colloid and Surface Science Symposium in Blacksburg, Virginia.
27. S. K. Friedlander, *Smoke, Dust, and Haze*, Wiley, New York (1977).